



# Electrodeposition and texture control of Ag-doped SnS thin films with high-electrical transmission properties

Sibo Hu<sup>1</sup> · Ying Liu<sup>1</sup> · Jingjun Liu<sup>1</sup> · Zhengping Zhang<sup>1</sup> · Jing Ji<sup>1</sup> · Zhilin Li<sup>1</sup> · Feng Wang<sup>1</sup>

Received: 5 October 2019 / Accepted: 26 December 2019 / Published online: 10 January 2020  
© Springer Science+Business Media, LLC, part of Springer Nature 2020

## Abstract

SnS is widely noticed in optoelectronics and thermoelectric fields. But the low-electrical transmission performance confines its actual application. In this paper, Ag-doped SnS thin films were successfully prepared by a simple electrodeposition method. The mechanism of the S and Sn co-deposition and the effect of complexing agent  $K_4P_2O_7$  were studied. The Ag content was successfully controlled by the adjustment of the electrolyte and deposition parameters. The *b*-axis texture was strengthened by Cetyl trimethyl ammonium bromide (CTAB) in the electrolyte. The carrier concentration was promoted by the control of Ag content and the carrier mobility was promoted by the strengthening of the *b*-axis texture. The electrical conductivity was promoted by the combination of the Ag concentration control and *b*-axis texture control. It reached the highest known value of  $1.40 \text{ S cm}^{-1}$  under the highest *b*-axis texture coefficient. Such a sample combination method and control strategies provide a new view for the preparation of semiconductors with high-electrical transmission properties.

## 1 Introduction

SnS received extensive attention in the field of optoelectronics [1, 2] because its optical band gap is very suitable for the solar spectrum [3] and it is comprised by abundant and inexpensive elements [4]. Recent studies have shown that the crystal structure of SnSe can effectively weaken phonon scattering, thus reducing the thermal conductivity of the material [5]. For this reason, SnSe showed the highest known thermoelectric figure of merit of 2.6 [6]. SnS has the same crystal structure, which implies that SnS should also have advantages in thermoelectric field [7]. On this condition, electrical transmission performance becomes a critical factor for the promotion of photoelectric and thermoelectric properties of SnS.

The electrical properties of the SnS are not satisfied for industry applications. Fortunately, they can be greatly

improved by element-doping [8]. It is reported that the carrier concentration of SnS doped with Na, Al, Pb, In, Cu and Ag was significantly increased [4, 9–12]. However, some shortcomings exist for the elements, so the selection of doping elements is very important. For instance, Na can only be incorporated into SnS in the form of intermediate compounds, which has harsh requirements on doping methods. Al itself is difficult to be incorporated into SnS. Pb is toxicity. In is a rare metal which is difficult to be extracted because it only exists in other metal ores as impurities. Both Cu and Ag do not have such shortcomings and limitations, but Cu was not as good as Ag in the improvement of the electrical transmission performance of SnS films [12]. In addition, Ag-doping can stabilize the Fermi energy level and enhance electron collection [13], so as to effectively improve the carrier concentration of the material. Therefore, Ag-doping of SnS attracted more and more attention.

However, high-carrier concentration is often accompanied by low mobility, which can be compensated by controlling crystal orientation [14, 15]. Studies indicated that SnSe with the same structure as that of SnS has high-electric conductivity along the *b*-axis, which is about ten times as high as that along the *a*-axis [5]. Therefore, we attempted to prepare SnS thin films with the *b*-axis texture on the basis of Ag-doping, so as to obtain samples with high-carrier concentration and mobility simultaneously.

✉ Zhilin Li  
lizl@mail.buct.edu.cn

✉ Feng Wang  
wangf@mail.buct.edu.cn

<sup>1</sup> State Key Laboratory of Chemical Resource Engineering, Beijing Key Laboratory of Electrochemical Process and Technology for Materials, Beijing University of Chemical Technology, Beijing 100029, People's Republic of China

Now, many methods were applied to prepare Ag-doped SnS thin films, such as chemical bath deposition [8, 16], electrodeposition [13], spark plasma sintering [17], spray pyrolysis [18] and vacuum thermal evaporation [19]. Among them, the electrodeposition method is noticeable for its simple equipment, mild reaction, easy control and low cost [20]. In this paper, we attempted one-step electrodeposition to prepare the SnS films with Ag-doping and *b*-axial texture, to adjust their band gap, carrier concentration and mobility for the promotion of their electric conductivity.

## 2 Experimental

### 2.1 Electrodeposition of undoped and Ag-doped SnS thin films

The electrolyte was comprised of 2 mMol l<sup>-1</sup> SnCl<sub>2</sub>, 16 mMol l<sup>-1</sup> Na<sub>2</sub>S<sub>2</sub>O<sub>3</sub> and 6 mMol l<sup>-1</sup> K<sub>4</sub>P<sub>2</sub>O<sub>7</sub>. Different amount of AgNO<sub>3</sub> was added into the electrolyte to reach the [Ag]/[Sn] ratio of 0–11%. CTAB solution of 1 mg/ml was added into 200 ml electrolyte with the amount of 0–3 ml to adjust the texture of the thin films. Substrate of indium-tin oxide (ITO) covered glass was ultrasonic cleaned in anhydrous ethanol and deionized water successively for 20 min. Electrodeposition was carried out potentiostatically with an electrochemical workstation (CHI 760E, China) in a conventional three electrode electrochemical cell with the stirring speed of 450r/min at 50 °C. The cell contained a saturated calomel electrode (SCE) as reference electrode and a platinum plate as auxiliary electrode. The working electrode was the ITO substrate. All the potentials mentioned in this paper are relative to the potential of saturated calomel electrode. The pH was adjusted to 3.0 using dilute H<sub>2</sub>SO<sub>4</sub>. After the electrodeposition, the samples were annealed at 350 °C for 30 min in a tubular furnace under the protection of Ar flow at a rate of 200–300 ml/min. The heating rate was controlled at 5 °C/min. Before the Hall effect test, the film was peeled off with marble glue to prevent the disturbance of ITO substrate on the electric transmission properties.

### 2.2 Characterization methods

Transmittance spectra were recorded by a UV–Vis spectrophotometer (ShimadzuUV-2450, Japan) in the wavelength range of 200–350 nm. An electrochemical workstation (CHI 760E, China) was used to test the cathode polarization curve and electrochemical impedance spectrum (EIS). The EIS plots were measured at a potential of -0.59 V in a frequency range of 100 kHz–0.1 Hz, and the disturbance amplitude was 10 mV. ZSimpWin software was used for equivalent circuit simulation. X-ray diffraction (XRD) spectra of the thin films were measured by an X-ray diffractometer (RINT 2200 V/

PC) with Cu K<sub>α</sub> radiation ( $\lambda = 0.15406$  nm) at 40 kV and 30 mA. The morphologies of the thin films were observed by a scanning electron microscope (SEM) (JEOL FE-JSM-6701F, Japan). The chemical composition of the thin films was investigated by an energy-dispersive X-ray (EDX) analyzer (Oxford INCA-Penta-FET-X3, England). The carrier type, concentration and mobility were determined by a Hall effect analyzer (Phys. Tech. RH2030).

## 3 Results and discussion

### 3.1 Electrodeposition of SnS thin films and its mechanism

#### 3.1.1 Co-deposition mechanism of SnS thin films

The linear polarization curves were tested in the solutions of SnCl<sub>2</sub>, Na<sub>2</sub>S<sub>2</sub>O<sub>3</sub>, SnCl<sub>2</sub> + Na<sub>2</sub>S<sub>2</sub>O<sub>3</sub>. The results are shown in Fig. 1. The curve in SnCl<sub>2</sub> solutions shows that the initial reduction potential of Sn<sup>2+</sup> was -0.50 V. And the curve in Na<sub>2</sub>S<sub>2</sub>O<sub>3</sub> solutions shows that the reduction of S<sub>2</sub>O<sub>3</sub><sup>2-</sup> started at the potential of -0.60 V. The difference of the reduction potential causes the difficulty of the co-deposition of Sn and S. The curve in the SnCl<sub>2</sub> + Na<sub>2</sub>S<sub>2</sub>O<sub>3</sub> solution shows two current peaks at -0.98 V and -1.08 V, which is believed corresponding to the reduction peak of Sn<sup>2+</sup> and S<sub>2</sub>O<sub>3</sub><sup>2-</sup>, respectively. Thus, it is difficult for the co-deposition of Sn and S to form SnS thin films with stoichiometry in this electrolyte system.

For better co-deposition, we attempted to introduce K<sub>4</sub>P<sub>2</sub>O<sub>7</sub> into the electrolyte to form complex with Sn<sup>2+</sup>, so that the reduction potential of Sn<sup>2+</sup> can be negatively shifted. The UV–Vis absorption spectra of the solutions of SnCl<sub>2</sub> and SnCl<sub>2</sub> + K<sub>4</sub>P<sub>2</sub>O<sub>7</sub> were tested, and the results are shown in Fig. 2. The absorption edge of Sn<sup>2+</sup> moves from

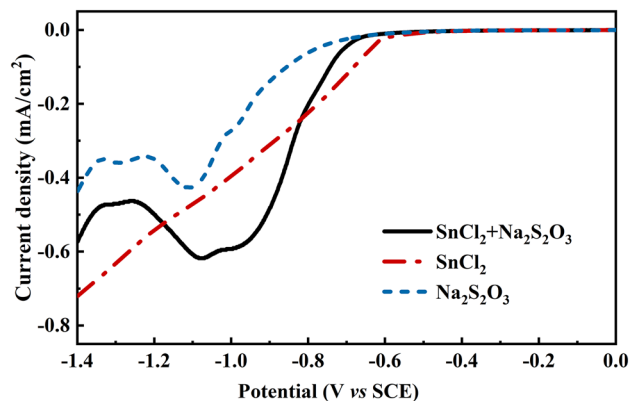


**Fig. 1** Linear polarization curves of the solutions of SnCl<sub>2</sub>, Na<sub>2</sub>S<sub>2</sub>O<sub>3</sub> and SnCl<sub>2</sub> + Na<sub>2</sub>S<sub>2</sub>O<sub>3</sub>

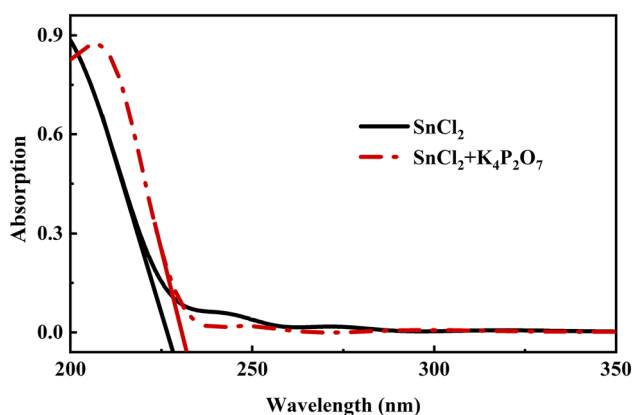


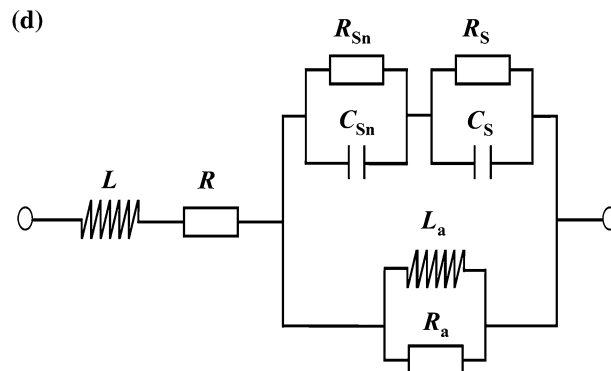
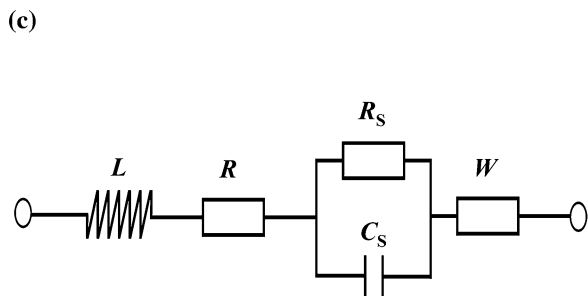
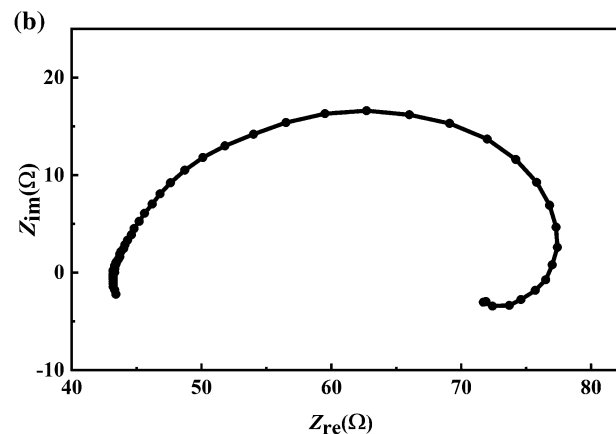
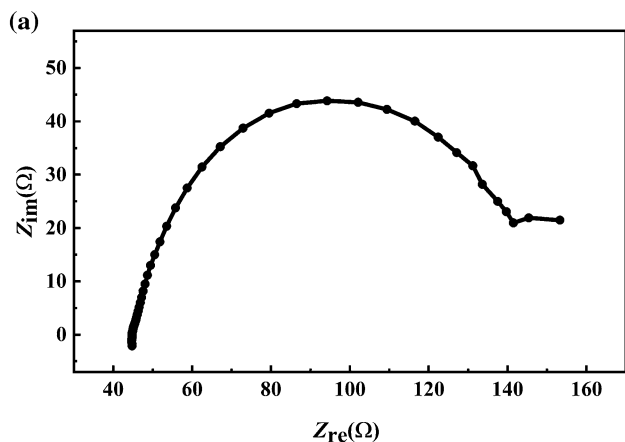
**Fig. 2** UV–Vis absorption spectra of the solutions of  $\text{SnCl}_2$  and  $\text{SnCl}_2 + \text{K}_4\text{P}_2\text{O}_7$

228 to 232.5 nm after the addition of  $\text{K}_4\text{P}_2\text{O}_7$ . The reason of such a red shift can be analyzed as follows. The electron configuration of  $\text{Sn}^{2+}$  is  $4d^{10}5s^2$ , and the vacant orbital exists at  $4d$  orbital [21]. Under acidic conditions,  $\text{K}_4\text{P}_2\text{O}_7$  will hydrolyze into  $\text{K}_2\text{P}_2\text{O}_7^{2-}$  [22]. The two oxygen atoms of  $\text{K}_2\text{P}_2\text{O}_7^{2-}$  will provide lone-pair electrons to the  $d$  orbital

of  $\text{Sn}^{2+}$  to form coordination bonds [23], so as to enhance conjugation effect and result in the red shift. The UV–Vis absorption spectra clearly show the formation of complex  $\text{Sn}(\text{K}_2\text{P}_2\text{O}_7)$  in the bath system.

The migration of the complex  $\text{Sn}(\text{K}_2\text{P}_2\text{O}_7)$  to the cathode can only adopt the path of diffusion, which is a slow process. After Sn reduction, the  $(\text{K}_2\text{P}_2\text{O}_7)^{2-}$  has to desorb from the cathode and diffuse into the solution, to provide deposition sites for the further reduction reaction on the cathode. The slow diffusion will cause concentration polarization to impede reduction of Sn and cause the negative shift of the reduction potential. Thus, the addition of  $\text{K}_4\text{P}_2\text{O}_7$  can restrain the deposition of Sn both thermodynamically and kinetically.

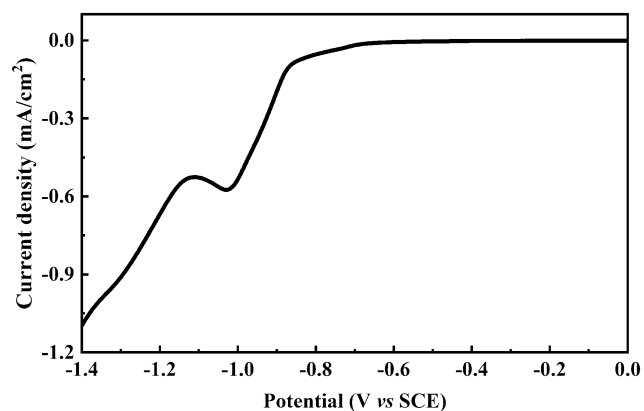
The EIS spectra of the solution system of  $\text{Na}_2\text{S}_2\text{O}_3 + \text{K}_4\text{P}_2\text{O}_7$  and  $\text{SnCl}_2 + \text{Na}_2\text{S}_2\text{O}_3 + \text{K}_4\text{P}_2\text{O}_7$  were tested, and the results are shown in Fig. 3. Their equivalent circuits are also shown in Fig. 3. The equivalent circuits were fitted according to the simulation on Zsimpwin software, and the value of the components are shown in Table 1. The equivalent circuit of the  $\text{Na}_2\text{S}_2\text{O}_3 + \text{K}_4\text{P}_2\text{O}_7$  system contains the solution reactance  $L$ , the solution resistance  $R$ , the double-layer capacitor  $C_S$  and the charge transfer resistance  $R_S$



**Fig. 3** EIS test results of the solution systems of **a**  $\text{Na}_2\text{S}_2\text{O}_3 + \text{K}_4\text{P}_2\text{O}_7$ , **b**  $\text{SnCl}_2 + \text{Na}_2\text{S}_2\text{O}_3 + \text{K}_4\text{P}_2\text{O}_7$ , and **c** equivalent circuit of (a), **d** equivalent circuit of (b)

**Table 1** EIS data obtained by equivalent circuit simulation of various solutions

Solution	$L$ (H)	$R$ ( $\Omega \text{ cm}^{-2}$ )	$R_S$ ( $\Omega \text{ cm}^{-2}$ )	$C_S$ (F $\text{cm}^{-2}$ )	$W$ (S $\text{sec}^{0.5} \text{ cm}^{-2}$ )	$R_{Sn}$ ( $\Omega \text{ cm}^{-2}$ )	$C_{Sn}$ (F $\text{cm}^{-2}$ )	$L_a$ (H)	$R_a$ ( $\Omega \text{ cm}^{-2}$ )
$\text{Na}_2\text{S}_2\text{O}_3 + \text{K}_4\text{P}_2\text{O}_7$	$4.08 \times 10^{-6}$	44.98	78.74	$1.46 \times 10^{-4}$	$1.33 \times 10^{-2}$	–	–	–	–
$\text{SnCl}_2 + \text{Na}_2\text{S}_2\text{O}_3 + \text{K}_4\text{P}_2\text{O}_7$	$4.03 \times 10^{-6}$	43.28	33.09	$1.27 \times 10^{-4}$	–	275.00	$1.56 \times 10^{-4}$	5.36	89.72

**Fig. 4** Cathodic polarization curve of  $\text{SnCl}_2 + \text{Na}_2\text{S}_2\text{O}_3 + \text{K}_4\text{P}_2\text{O}_7$  solution system

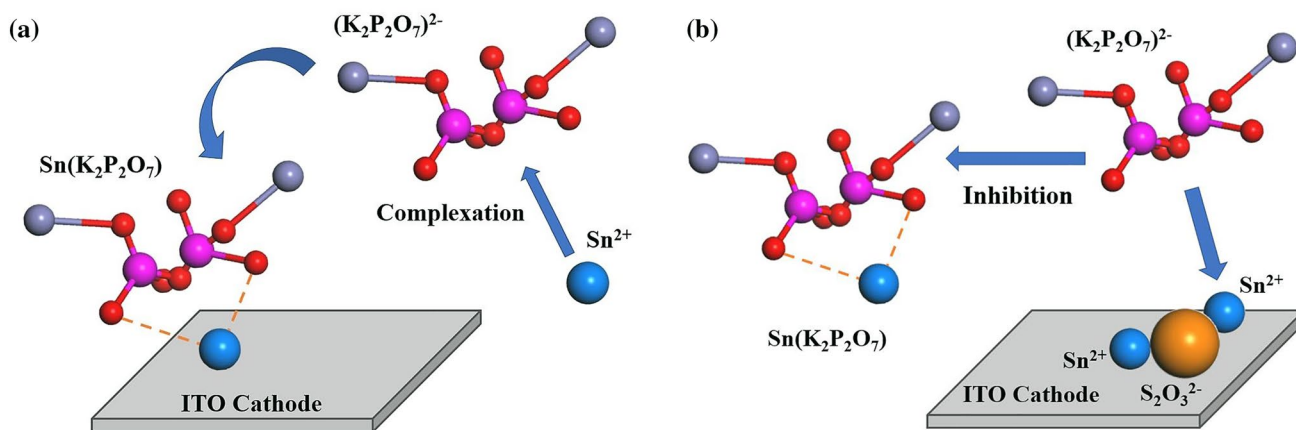
cause by S, and the warburg impedance  $W$ . The equivalent circuit of the  $\text{SnCl}_2 + \text{Na}_2\text{S}_2\text{O}_3 + \text{K}_4\text{P}_2\text{O}_7$  system contains the solution reactance  $L$ , the solution resistance  $R$ , resistance  $R_a$  and reactance  $L_a$  caused by the cathode adsorption of  $\text{Sn}(\text{K}_2\text{P}_2\text{O}_7)$  and the desorption of  $(\text{K}_2\text{P}_2\text{O}_7)^{2-}$  [24], the charge transfer resistances  $R_{Sn}$ ,  $R_S$  and double-layer capacitor  $C_{Sn}$ ,  $C_S$  which are caused by Sn and S, respectively.

It can be seen that the charge transfer resistance  $R_S$  in the  $\text{Na}_2\text{S}_2\text{O}_3 + \text{K}_4\text{P}_2\text{O}_7$  system was  $78.74 \Omega \text{ cm}^{-2}$ , and it reduced to  $33.09 \Omega \text{ cm}^{-2}$  in the  $\text{SnCl}_2 + \text{Na}_2\text{S}_2\text{O}_3 + \text{K}_4\text{P}_2\text{O}_7$  system. Thus, the addition of  $\text{Sn}^{2+}$  can induce the reduction

of  $\text{S}_2\text{O}_3^{2-}$ , which is advantageous to the co-deposition of Sn and S. It should be noticed in Fig. 3b and d that the electrochemical impedance directly caused by Sn ( $R_{Sn}/C_{Sn}$ ) and S ( $R_S/C_S$ ) is in parallel with ( $R_a/L_a$ ), which indicates that the adsorption and desorption lasted during the whole deposition process. It further proves that the  $\text{Sn}^{2+}$  and  $\text{S}_2\text{O}_3^{2-}$  were reduced simultaneously and the co-deposition was accomplished by the inducing effect of Sn and the complex effect of  $\text{K}_4\text{P}_2\text{O}_7$ .

Figure 4 shows the cathodic polarization curve of the electrolyte after addition of  $\text{K}_4\text{P}_2\text{O}_7$ . It can be seen that the two reduction peaks of  $\text{SnCl}_2 + \text{Na}_2\text{S}_2\text{O}_3$  solution in Fig. 1 now merged into one at  $-1.02 \text{ V}$ , which is advantageous to the co-deposition. Such result is in well accordance with the results of UV–Vis spectra and EIS and further proves the inducing effect of Sn and the complex effect of  $\text{K}_4\text{P}_2\text{O}_7$ .

Up to now, the co-deposition process of SnS thin films can be summarized as follows. First, the complex  $\text{Sn}(\text{K}_2\text{P}_2\text{O}_7)$  formed by  $(\text{K}_2\text{P}_2\text{O}_7)^{2-}$  and  $\text{Sn}^{2+}$  ions in the electrolyte and diffused to the cathode surface. The  $\text{Sn}^{2+}$  ions were then reduced by the cathode and deposited on the cathode surface.  $(\text{K}_2\text{P}_2\text{O}_7)^{2-}$  ions then separated with Sn atom and desorbed. Such process is shown in Fig. 5a. The desorbed  $(\text{K}_2\text{P}_2\text{O}_7)^{2-}$  ions would defused back the electrolyte and obstruct the further diffusion of the complex  $\text{Sn}(\text{K}_2\text{P}_2\text{O}_7)$  to the cathode. Such process is shown in Fig. 5b. So, the deposition of Sn was inhibited. On the other hand, the deposited Sn would promote the reduction of  $\text{S}_2\text{O}_3^{2-}$ ,

**Fig. 5** Schematic diagram of the co-deposition mechanism of SnS. **a** formation of the complex and its absorption on the cathode, and **b** the inhibition of  $\text{Sn}^{2+}$  reduction and the induction of  $\text{S}_2\text{O}_3^{2-}$  reduction

and finally generate SnS. Such a process is also shown in Fig. 5b. Through such a mechanism, the reduction of Sn was inhibited and the reduction of  $S_2O_3^{2-}$  was promoted, so the co-deposition of SnS was accomplished.

### 3.1.2 Actual effect of $K_4P_2O_7$ on the co-deposition of SnS thin films

The deposition of SnS thin films was executed on the following conditions: deposition potential of  $-0.9$  to  $-1.1$  V, deposition time of 40 min, stirring speed of 450r/min. The compositions of the thin films deposited with and without  $K_4P_2O_7$  were tested by EDX, and the results are shown in Table 2. It can be seen that the compositions of the SnS thin films deposited with  $K_4P_2O_7$  were closer to the stoichiometry than that of the SnS thin films deposited without  $K_4P_2O_7$  at all deposition potentials. The advantageous effect of  $K_4P_2O_7$  on the co-position is verified here.

The XRD and SEM test results of the SnS thin films deposited with  $K_4P_2O_7$  at  $-1.1$  V after the annealing are shown in Fig. 6. All the peaks of Fig. 6a correspond well with the diffraction peak of orthorhombic SnS except those

**Table 2** Composition of the SnS thin films deposited with and without  $K_4P_2O_7$

Deposition potential (V)	$K_4P_2O_7$ content ( $mMol\ l^{-1}$ )	Composition (at.%)		[S]/[Sn]
		[S]	[Sn]	
-0.9	–	41.40	58.60	0.71
	6	43.95	56.05	0.78
-1.0	–	44.44	55.56	0.80
	6	45.39	54.60	0.83
-1.1	–	53.74	46.26	1.16
	6	46.40	53.60	0.87

from the diffraction of the ITO substrate, so the thin films should be composed by SnS. It should be noticed that some other compounds, such as  $SnS_2$  and  $Sn_2S_3$ , are difficult to be distinguished from orthorhombic SnS because some of the positions of their XRD peaks are quite close [25, 26]. Thus, a little amount of secondary phases probably exist in the thin films. However, such little amount of probable secondary phases did not have noticeable influence on the electrical transmission properties, so we did not research them further.

It can be seen from Fig. 6b that the thin film was compact and homogeneous. Cross-section observation showed the thickness of the thin film was in the range of 551–671 nm depending on the deposition conditions. Satisfying SnS thin films were obtained through the research of the co-deposition mechanism.

## 3.2 Preparation and electric transmission properties of Ag-doped SnS thin films

### 3.2.1 Composition and texture control of Ag-doped SnS thin films

Different amount of  $AgNO_3$  was added into the electrolyte to prepare the Ag-doped SnS thin films at the potential of  $-1.1$  V. The composition of the obtained thin films are shown in Table 3. It was believed that the dopant cation should be  $Ag^{2+}$  [27]. It can be seen that the Ag content of the thin films increased with the increase of  $[Ag]/[Sn]$  in the electrolyte. The largest Ag-doping content reached as high as 3.85 at%. The atomic ratio of  $[S]/\{[Sn] + [Ag]\}$  has no direct relation to the amount of Ag. The ratio fluctuated between 0.81 and 0.94, which was close to the stoichiometry of 1. So the Ag-doping content could be well controlled within reasonable  $[S]/\{[Sn] + [Ag]\}$  ratio.

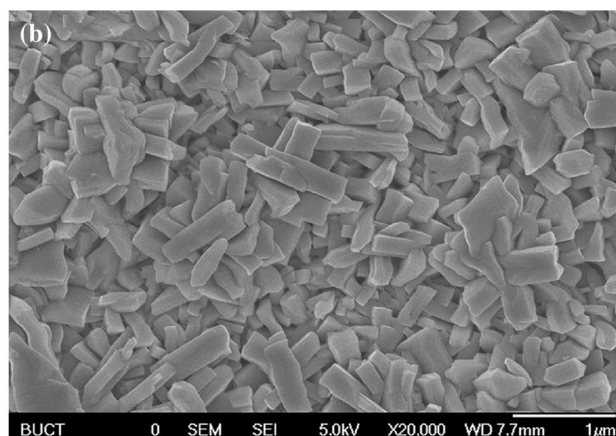
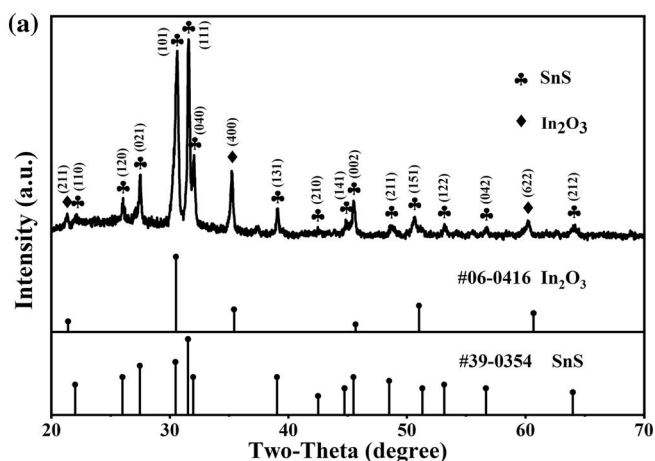


**Fig. 6** XRD and SEM test results of the SnS thin films deposited with  $K_4P_2O_7$  at  $-1.1$  V after the annealing. **a** XRD, and **b** SEM



**Table 3** Composition of Ag-doped SnS thin films

[Ag]/[Sn] in the electrolyte (%)	Composition of the thin films (at.%)			[S]/{[Sn] + [Ag]}
	[S]	[Sn]	[Ag]	
0	46.85	53.15	0	0.88
0.5	45.94	53.69	0.37	0.85
1.0	46.24	53.13	0.63	0.86
1.5	45.69	53.48	0.83	0.84
2.0	46.90	52.01	1.09	0.88
2.5	45.26	53.72	1.02	0.83
5.0	45.53	53.25	1.22	0.84
7.0	44.61	54.19	1.20	0.81
9.0	48.57	49.33	2.10	0.94
11.0	45.32	50.83	3.85	0.83

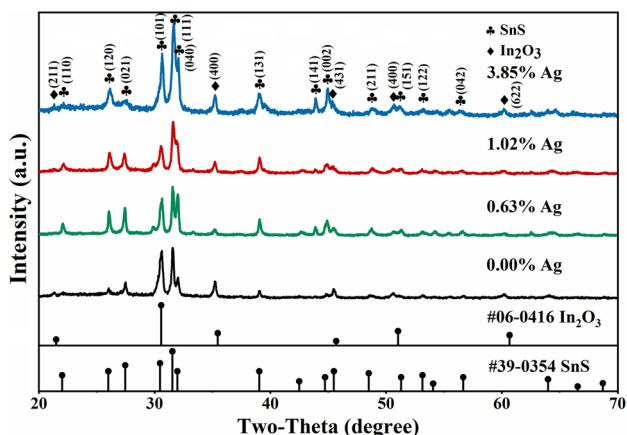


**Fig. 7** XRD results of the Ag-doped thin films with different Ag content

Figure 7 shows the XRD results of the Ag-doped thin films with different Ag content. All the peaks corresponds to the diffraction of orthorhombic SnS except those corresponding to the ITO substrate. Therefore, the Ag-doping did not change the orthorhombic crystal structure of pure SnS because it almost did not change the [S]/[Sn] ratio. Because the atom radius of Ag is smaller than that of Sn, the crystal cell volume of SnS should contract when Ag atom replace Sn atom in the SnS lattice. Furthermore, the contraction will increase when the Ag content increases [27]. We calculated the cell volume of the Ag-doped SnS thin films with different Ag content according to the XRD results, the calculation results are shown in Table 4. It can be seen that the relationship between the cell volume and Ag content was just in well accordance with above deduction. The cell volume contraction proves the formation of Ag-doped SnS thin films.

It should be noticed that all the relative strengths of the (040) peaks ( $2\theta$  is close to  $31.971^\circ$ ) of the thin films are

**Table 4** Lattice parameters and crystal cell volume  $V$  calculated from the XRD results

Ag at. %	Lattice parameter (nm)			$V$ (nm <sup>3</sup> )
	$a$	$b$	$c$	
–	0.4332	1.1178	0.3984	0.1929
0.63	0.4318	1.1189	0.3989	0.1927
1.02	0.4298	1.1210	0.3981	0.1922
3.85	0.4312	1.1133	0.3988	0.1914

**Table 5** Texture coefficient of (040) of SnS and Ag-doped thin films

Ag at. %	Texture coefficient
–	1.83
0.63	2.47
1.02	2.43
3.85	2.64

higher than that in the standard card (JCPDS39-0354), so all the thin films had the (040) texture ( $b$ -axis). Such a texture is supposed being profitable for the electron transfer in such a crystal structure, which is similar to the case in single crystal SnSe [5].

In order to compare the extent of texture of (040), we calculated the  $b$ -axis texture coefficient  $T_{040}$  of a thin film with [3]

$$T_{040} = \frac{I_{040}/I_{040}^0}{\frac{1}{n} \sum_{i=1}^n I_{HKL}/I_{HKL}^0} \tag{1}$$

where  $I_{HKL}$  represents the tested relative strength of the diffraction peak of any ( $HKL$ ) crystal plane,  $I_{HKL}^0$  represents the standard relative strength of the diffraction peak of the same ( $HKL$ ) crystal plane,  $I_{040}$  represents the tested relative strength of the diffraction peak of (040) crystal plane,  $I_{040}^0$  represents the standard relative strength of the diffraction peak of (040) crystal plane, and  $n$  represents the total number of reflections. In our case,  $n = 16$ . The calculation results are shown in Table 5. Although (040) texture existed in the SnS thin film, the texture coefficient increased obviously after the Ag-doping.

To further promote the carrier mobility of the Ag-doped SnS thin films, we attempted to strengthen the (040) texture of the Ag-doped SnS thin films. We introduced 0–3 ml CTAB with the concentration of 1 mg/ml into the 200 ml electrolyte with [Ag]/[Sn] ratio of 11.0%. The XRD results of the thin films deposited in such electrolytes are shown in Fig. 8. It can be seen that the thin films still had the orthorhombic crystal structure of SnS and all of them had obvious (040) texture. The (040) texture coefficient were also calculated and the results are shown in Table 6. It can be

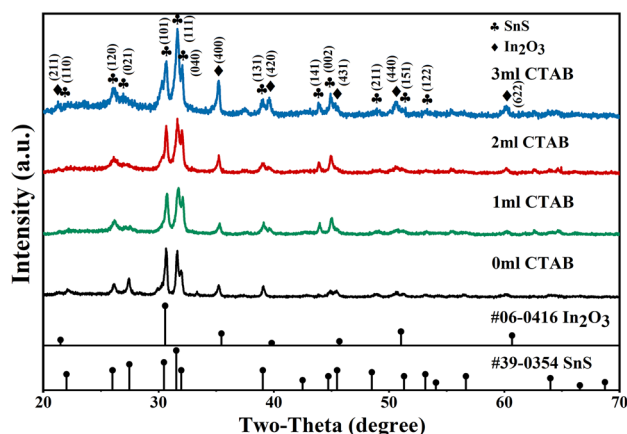


**Fig. 8** XRD spectra of the Ag-doped SnS thin films deposited in the electrolytes with [Ag]/[Sn] ratio of 11.0% and different CTAB adding amount

**Table 6** Influence of CTAB amount on (040) texture coefficient of the Ag-doped SnS thin films

Amount of CTAB (ml)	<i>b</i> -Axis texture coefficient
–	2.64
1	2.96
2	3.27
3	2.67

seen that CTAB had obvious influence on the texture coefficient. The texture coefficient reached the maximum value of 3.27 at the CTAB amount of 2 ml. Therefore, the *b*-axis texture of the Ag-doped SnS thin films were successfully strengthened by the addition of CTAB. The SEM image of Ag-doped SnS thin film deposited with 2 ml CTAB is shown in Fig. 9. It can be seen compact and homogeneous morphology of the thin film still sustained after the Ag-doping and texture strengthening. Such morphology is profitable for the electron transformation.

### 3.2.2 Relationship between Ag content, texture and electric transfer properties of Ag-doped SnS thin films

The Hall effect test results of the SnS thin films with different Ag content are shown in Table 7. The results show that the thin films were still p-type semiconductors after the Ag-doping. The carrier concentration increased violently with the increase of Ag content in the thin films, and it reached the maximum value of  $1.87 \times 10^{20} \text{ cm}^{-3}$  at the Ag content of 3.85-at%. But the carrier mobility decreased meanwhile, which is consistent with the theoretical result [28]. As a result, the electric conductivity of the Ag-doped SnS thin films reached the maximum value at the Ag content range

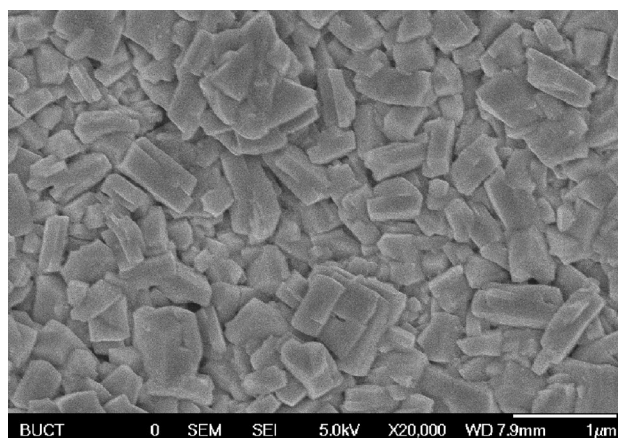


**Fig. 9** SEM image of Ag-doped SnS thin film deposited with 2 ml CTAB

**Table 7** Influence of Ag content on electric transmission properties of Ag-doped SnS thin films (300 K)

Ag-at%	Carrier concentration ( $\text{cm}^{-3}$ )	Carrier mobility ( $\text{cm}^2/\text{Vs}$ )	Electrical conductivity ( $\text{S cm}^{-1}$ )
–	$9.66 \times 10^{15}$	2.44	$3.78 \times 10^{-3}$
0.63	$2.57 \times 10^{16}$	1.59	$6.58 \times 10^{-3}$
1.02	$7.70 \times 10^{16}$	1.16	$1.43 \times 10^{-2}$
2.10	$7.42 \times 10^{17}$	1.15	0.137
3.85	$1.87 \times 10^{20}$	$4.59 \times 10^{-3}$	0.138

of 2.1–3.85 at.%. In other words, the profitable effect of Ag on the conductivity would no longer exert because of the decrease of the carrier mobility when the Ag content was too high. Therefore, other measurement should be attempted to increase the conductivity further.

As discussed above, the (040) texture of the Ag-doped SnS thin films was strengthened by the addition of CTAB. The Hall effect test results of the thin films with different amounts of CTAB are listed in Table 8. It can be seen that the electrical conductivity of the Ag-doped SnS thin films increased further after the CTAB addition, although the carrier concentration decreased slightly. It is clearly shown that the carrier mobility of the thin films increased when the *b*-axis texture coefficient increased. Too high CTAB amount of 3 ml caused low *b*-axis texture coefficient of 2.67, the carrier mobility of the thin films decreased correspondingly. Thus, the increase of conductivity clearly connected to the increase of the texture coefficient of (040) crystal plane. The advantageous effect of *b*-axis orientation was reasonably analyzed theoretically and proved experimentally. Our results is in well accordance with such results.

It should be mentioned that the electrical conductivity reached the maximum value of  $1.40 \text{ S cm}^{-1}$  under the CTAB

**Table 8** Hall effect test results of the Ag-doped SnS thin films deposited in the electrolyte with [Ag]/[Sn] ratio of 11.0% and different amount of CTAB (300 K)

CTAB amount (ml)	Carrier concentration (cm <sup>-3</sup> )	Carrier mobility (cm <sup>2</sup> /Vs)	Electrical conductivity (S cm <sup>-1</sup> )	(040) Texture coefficient
–	1.87 × 10 <sup>20</sup>	4.59 × 10 <sup>-3</sup>	0.14	2.64
1	2.17 × 10 <sup>18</sup>	1.00	0.35	2.96
2	1.57 × 10 <sup>18</sup>	5.58	1.40	3.27
3	8.73 × 10 <sup>18</sup>	0.25	0.34	2.67

amount of 2 ml which determined the highest (040) texture coefficient of 3.27. Such value is the largest one as far as we know among the Ag-doped SnS thin films prepared with different methods [8, 16, 18, 29–31].

Up to now, we successfully promoted the carrier concentration of the SnS thin films by Ag-doping and promoted the carrier mobility by *b*-axis texture strengthening. The electrical conductivity was promoted by the combination of the Ag concentration control and *b*-axis texture coefficient control through a sample electrodeposition method. Such a sample combined method and control measurements provide a new view for the preparation of semiconductors with high-electrical transmission properties.

## 4 Conclusions

Ag-doped SnS thin films were successfully prepared by electrodeposition method. The mechanism of the S and Sn co-deposition and the effect of complexing agent K<sub>4</sub>P<sub>2</sub>O<sub>7</sub> were studied. The Ag content was controlled by the adjustment of the electrolyte and deposition parameters on the basis of the mechanism analysis. The (040) texture was strengthened by the addition of CTAB into the electrolyte. The carrier concentration of the Ag-doped thin films was promoted by the control of Ag content and the carrier mobility was promoted by the strengthening of (040) texture. The electrical conductivity was promoted by the combination of the Ag concentration control and *b*-axis texture coefficient control. It reached highest known value of 1.40 S cm<sup>-1</sup> under the highest (040) texture coefficient which determined the highest carrier mobility. Such a sample combination method and control measurements provide a new view for the preparation of semiconductors with high-electrical transmission properties.

**Acknowledgement** The authors acknowledge the financial support from National Natural Science Foundation of China (Grant No. 51472020).

## References

1. F. Jiang, H. Shen, W. Wang, L. Zhang, J. Electrochem. Soc. **159**, 235 (2012)
2. J. Xu, Y. Yang, Z. Xie, J. Mater. Sci: Mater Electron. **25**, 3028 (2014)
3. M. Kul, J. Vacuum **107**, 213 (2014)
4. M. Seal, N. Singh, E.W. McFarland, J. Baltrusaitis, J. Phys. Chem. C **119**, 6471 (2015)
5. L.D. Zhao, S.H. Lo, Y. Zhang, H. Sun, G. Tan, C. Uher, C. Wolverton, V.P. Dravid, M.G. Kanatzidis, Nature **508**, 373 (2014)
6. L.D. Zhao, G. Tan, S. Hao, J. He, Y. Pei, H. Chi, H. Wang, S. Gong, H. Xu, V.P. Dravid, C. Uher, G.J. Snyder, C. Wolverton, M.G. Kanatzidis, Science **351**, 141 (2016)
7. B.Z. Sun, Z.J. Ma, C. He, K.C. Wu, RSC. Adv. **5**, 56382 (2015)
8. S. Gedi, V.R.M. Reddy, T.R.R. Kotte, S.H. Kim, C.W. Jeon, Ceram. Int. **42**, 19027 (2016)
9. V. Steinmann, R.E. Brandt, R. Chakraborty, R. Jaramillo, M. Young, B.K. Ofori-Okai, C. Yang, A. Polizzotti, K.A. Nelson, R.G. Grodon, T. Buonassisi, APL. Mater. **4**, 026103 (2016)
10. H. Kafashan, R.E. Kahrizsangi, F.J. Sheini, R. Yousefi, Phys. Status Solidi A **213**, 1302 (2016)
11. S. Hao, V.P. Dravid, M.G. Kanatzidis, C. Wolverton, APL Mater. **4**, 104505 (2016)
12. Y. Liu, K. Cao, J. Liu, Z. Zhang, J. Ji, F. Wang, Z. Li, J. Mater. Sci: Mater. Electron. **30**, 15880 (2019)
13. M.A. Almessiere, A.L. Al-Otaibi, I.B. Assaker, T. Ghrib, R. Chtourou, Mater. Sci. Semicond. Process. **40**, 267 (2015)
14. D. Kong, H. Wang, J.J. Cha, M. Pasta, K.J. Koski, J. Yao, Y. Cui, Nano Lett. **13**, 1341 (2013)
15. S.M. Herron, J.T. Tanskanen, K.E. Roelofs, S.F. Bent, Chem. Mater. **26**, 7106 (2014)
16. L. Yeh, K. Cheng, J. Power Sources **275**, 750 (2015)
17. Q. Tan, L.D. Zhao, J.F. Li, C.F. Wu, T.R. Wei, Z.B. Xing, M.G. Kanatzidis, J. Mater. Chem. A. **2**, 17302 (2014)
18. K.S. Kumar, A.G. Manohari, S. Dhanapandian, T. Mahalingam, Mater. Lett. **131**, 167 (2014)
19. H.J. Jia, S.Y. Cheng, X.K. Wu, Y.L. Yang, Nat. Sci. **2**, 197 (2010)
20. C. An, K. Tang, Y. Jin, Q. Liu, X. Chen, Y. Qian, J. Cryst. Growth **252**, 581 (2003)
21. A. Tang, J. Liu, M. Dou, Z. Li, F. Wang, Appl. Surf. Sci. **383**, 253 (2017)
22. J. Fang, *Plating Compound: Theory and Application*, 1st edn. (Chemical Industry Press Co. Ltd., Beijing, 2008), pp. 347–349 (in Chinese)
23. A. Adam, S. Verma, G. Seth, Eur. J. Chem. **8**, 404 (2011)
24. X. Xu, F. Wang, J. Liu, J. Ji, Electrochim. Acta **55**, 4428 (2010)
25. B.H. Baby, D.B. Mohan, Sol. Energy. **174**, 373 (2018)
26. B.H. Baby, D.B. Mohan, Sol. Energy. **189**, 207 (2019)
27. B.H. Baby, D.B. Mohan, Sol. Energy. **193**, 61 (2019)
28. Z. Li, *Material Physics*, 2nd ed. (Chemical Industry Press Co. Ltd, 2015), pp. 154 (in Chinese)
29. M. Devika, N.K. Reddy, K. Ramesh, K.R. Gunasekhar, E.S.R. Gopal, K.T.R. Reddy, J. Electrochem. Soc. **153**, 727 (2006)
30. P. Lu, H. Jia, S. Cheng, Adv. Mater. Res. **60**, 11 (2009)
31. H. Jia, S. Cheng, P. Lu, Adv. Mater. Res. **152**, 752 (2011)

**Publisher's Note** Springer Nature remains neutral with regard to jurisdictional claims in published maps and institutional affiliations.